JOURNAL OF
APPLIED
CRYSTALLOGRAPHY

ISSN 1600-5767

Residual strain orientation in rolled titanium determined with synchrotron X-ray Laue microdiffraction

Michelle Devoe,[a]* Nobumichi Tamura[b] and Hans-Rudolf Wenk[a]

[a]Earth and Planetary Science, University of California, Berkeley, CA 94720, USA, and [b]Advanced Light Source, Lawrence Berkeley National Laboratory, Berkeley, CA 94720, USA. *Correspondence e-mail: mdevoe@berkeley.edu

Received 10 October 2022
Accepted 23 November 2022

Edited by J. Keckes, Montanuniversität Leoben, Austria

Keywords: stress; strain; residual stress; residual strain; X-ray synchrotron radiation; Laue diffraction.

Previously, synchrotron X-ray Laue microdiffraction has been used to measure the magnitudes of residual strain in materials. Recently the method was advanced to determine the orientation of the strain ellipsoid and applied to naturally deformed quartzites; however, the deformation history of these quartzites is ambiguous due to their natural origin. In this study, synchrotron X-ray Laue microdiffraction (µXRD) is used to measure the residual strain for the first time in a sample with known stress history, rolled titanium. A deviatoric strain tensor is calculated from each Laue diffraction image collected with two µXRD scans of a rolled titanium sheet in different sample orientations. The principal strain axes are calculated using an eigen decomposition of the deviatoric strain tensors. The results show that the principal axis of compression is aligned with the normal direction of the titanium sheet, and the principal axis of extension is aligned with the rolling direction. Pole figures are used to represent the 3D distribution of residual strain axes.

1. Introduction

Residual stress has been of interest to metallurgists and structural engineers for decades (*e.g.* Noyan & Cohen, 1987). It affects the strength of metals and welds, and is significant for the stability of ships, pipelines and bridges (*e.g.* Hosford, 2005; Withers, 2007; Van Puymbroeck *et al.*, 2019) and the strength of thin films (*e.g.* Noyan *et al.*, 1995; Ma *et al.*, 2012). Residual stress can be introduced into a material at any point during fabrication and processing from mechanical working or heat treatment, and thus its characterization is key to understanding not only the quality of the material but also the effects of the manufacturing process on material properties.

Residual strain is a change to the lattice geometry of a crystalline material as a result of deformation or thermal changes. Residual strain, which remains in the material after the external force has been removed, can be categorized as plastic strain, which manifests as dislocations that disrupt the periodicity of the crystalline lattice, or elastic strain, which describes the shape distortion of the crystal lattice surrounding dislocations (Noyan & Cohen, 1987). These strains are related to stress through Hooke's law. Many techniques have been developed to detect and measure strain in metals (*e.g.* Schajer, 2013). Bulk properties can be measured with neutron diffraction due to its great penetration depth (Krawitz & Holden, 1990; Robinson *et al.*, 2017; Noyan *et al.*, 2020; Wissink *et al.*, 2020). X-ray diffraction (XRD) has been used as a nondestructive method (Ungár & Borbély, 1996; Ungár *et al.*, 2001; Cauchois *et al.*, 2014). Single-crystal properties can be measured using synchrotron X-ray microdiffraction (µXRD) (Tamura *et al.*, 2002; Levine *et al.*, 2006;

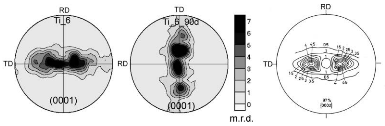

https://doi.org/10.1107/S1600576722011311

Renversade & Borbély, 2017; Morawiec, 2018). µXRD utilizes a micro-focused polychromatic X-ray beam from a synchrotron X-ray source with a diameter of ∼0.1–1 µm to raster scan a crystalline material over a large area (millimetres) and collect 2D Laue images at each step. The subsequent analysis generates high-resolution strain maps of polycrystalline materials (Spolenak *et al.*, 2003; Ice *et al.*, 2005*a*; Hofmann *et al.*, 2010; Kwon *et al.*, 2013; Jiang *et al.*, 2014; Qian *et al.*, 2017). If the grain size is larger than the beam diameter and step size, strain differentials may be resolved across grain boundaries (Spolenak *et al.*, 2003).

For the past 10 years, we have analyzed the orientation of macrostresses responsible for residual strain in natural quartzite using µXRD and have found results consistent with the stress history presumed from geological events. We developed a methodology to represent the 3D orientation of residual strain axes with pole figures generally used for crystal orientations or textures (Chen *et al.*, 2011, 2016; Li *et al.*, 2020; Wenk *et al.*, 2020). However, geological materials have a complex stress history, enduring a variety of stresses over long time scales, and thus there remains some uncertainty about their presumed stress history. Therefore, we decided to test µXRD and our experimental and analytical approach on a simple metal with a known deformation history to verify the accuracy of the results.

Studies looking at directionality of residual strain in metals have been primarily focused on cubic metals (Spolenak *et al.*, 2003; Shen *et al.*, 2022). In this study, we determine the directionality of the residual strain tensor of a hexagonal metal, titanium, with µXRD. The strength, corrosion resistance, and other mechanical and chemical properties of Ti and its alloys make them useful in a number of engineering sectors, including aerospace, nuclear, automotive and bioengineering (*e.g.* Lütjering & Williams, 2007; Mehta *et al.*, 2007; Wang *et al.*, 2020), and the microstructures and textures of Ti and Ti alloys have been well characterized (Partridge, 1967; Blicharski *et al.*, 1979; Zaefferer, 2003; Lonardelli *et al.*, 2007; Britton *et al.*, 2015; Guo *et al.*, 2015). We present strain maps and 3D orientation distributions of the residual strain tensor, equivalent stress calculations, and the deformation texture of rolled Ti derived from µXRD data.

Figure 1
Scanning electron microscope backscatter electron image of the cross section of rolled titanium. RD is rolling direction, ND is normal direction.

2. Experimental methodology

A 1.2 mm-thick sheet of ASTM B 295 Grade 4 commercially pure rolled Ti was cut into a 1.8 × 1.4 cm piece used for analysis. The sample grain size ranges from 5 to 30 µm. Grains appear to be flattened with a long axis parallel to the rolling direction (RD) (Fig. 1).

2.1. X-ray Laue microdiffraction

X-ray Laue microdiffraction measurements were conducted at beamline 12.3.2 of the Advanced Light Source (ALS) at Lawrence Berkeley National Laboratory. The methodology has been previously described (Tamura, 2014; Chen *et al.*, 2016; Li *et al.*, 2020; Wenk *et al.*, 2020). The 1.8 × 1.4 × 0.12 mm Ti sample was loaded onto a translational stage. The stage was tilted 45° to the incident X-ray beam [Fig. 2(*a*)]. A polychromatic X-ray beam with an energy range of 5 to 24 keV was collimated to a spot size of 1 µm in diameter. The rolled surface, perpendicular to the normal direction (ND), of the Ti sample was placed at the focal point of the X-ray beam using a laser proxy. The translational stage then rastered across the X-ray beam at the user-set step size and scan dimensions, which are programmed using the beamline control software. 2D diffraction images [Fig. 2(*b*)] were collected at each step by a Dectris Pilatus 1M detector positioned at 90° to the incident beam. The maximum penetration depth is 100 µm (source https://www.cxro.lbl.gov/).

A single crystal of silicon was crushed into grains ranging in size from 0.05 to 2 mm; these were mounted on a glass slide with double-sided sticky tape and used as a calibrant. This is different from previous experiments which used a single crystal of silicon or synthetic quartz (Chen *et al.*, 2016; Wenk *et al.*, 2020). The multiple peaks generated from a polycrystalline calibrant [Fig. 3(*a*)] eliminate the orientation bias that is introduced into the strain analysis from the use of a single-crystal calibrant, which only has a few peaks on each detector

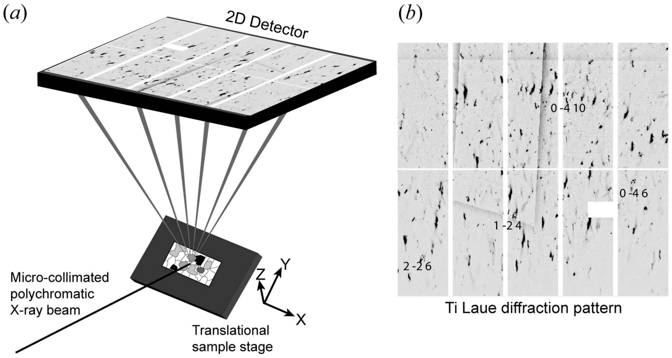

Figure 2
(*a*) Schematic of beamline experimental geometry at ALS 12.3.2 showing the polycrystalline Ti sample on the translational stage. The Dectris Pilatus 1M area detector located 90° above the incident X-ray beam collects a diffraction image. (*b*) Example Ti X-ray Laue diffraction image. A few exemplary peaks have been assigned Miller indices. White lines are interstitial space between detector panels. The white rectangle in the bottom right is a defective submodule that has been removed from analysis. The dark vertical shadow is the boundary of Kapton tape used to repair the detector.

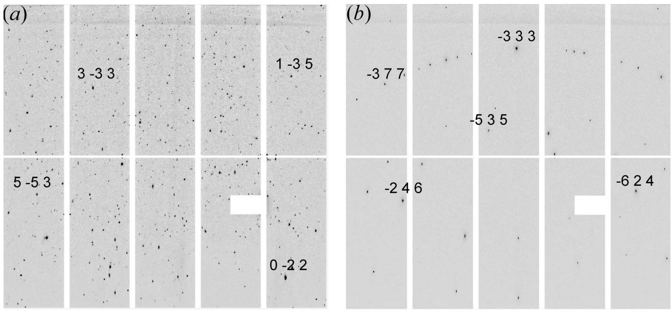

Figure 3
X-ray Laue diffraction images of (*a*) polysilicon calibrant and (*b*) single-crystal silicon calibrant. A few exemplary peaks have been assigned Miller indices. White lines are interstitial space between detector panels. The white rectangle is a defective submodule that has been removed from analysis.

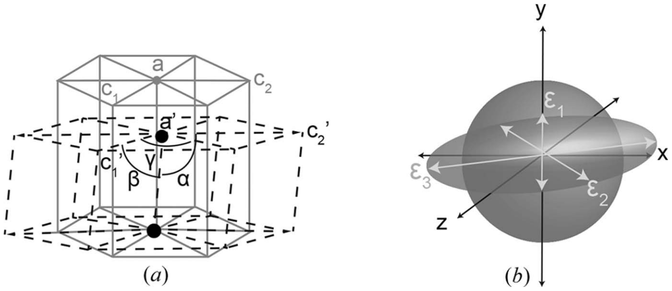

Figure 4
(*a*) Hexagonal unit cell (solid lines, lattice parameters a, c_1, c_2) distorted into a new triclinic shape (dashed lines, lattice parameters a', c_1', c_2', α, β, γ). (*b*) A sphere is distorted into a strain ellipsoid to represent the distortion shown in (*a*). Strain ellipsoid axes (ε_1, ε_2, ε_3) are noted relative to sample coordinate axes (x, y, z).

panel [Fig. 3(*b*)]. The calibration is used in data processing and does not affect the data collection.

An area of 1500 × 2000 µm on the rolled surface of the Ti sample was scanned with the X-ray beam in 50 µm steps to cover a large area for good grain statistics (scan Ti_6). While a 1 µm step size is achievable at beamline ALS 12.3.2, the grain size of the sample ranged from 5 to 30 µm and thus use of a 1 µm step size would sample a very limited number of grains during a reasonable collection time period. Thus, a larger step size of 50 µm was chosen to measure a large number of grains and collect data more representative of the whole sample. The exposure time was 1 s and the scan took approximately 20 min to complete. Since the maximum penetration depth of X-rays is 100 µm, approximately 1/12 of the depth profile of the rolled Ti sheet was sampled. The sample was then rotated 90° and approximately the same area was re-scanned (scan Ti_6_90d). The purpose of this repeated scan is to verify that the orientation of residual strain rotates with sample rotation, demonstrating that the strain measured is not an artifact due to calibration geometry uncertainties and other errors.

2.2. Data analysis overview

A more detailed explanation of data analysis has been published by Tamura (2014) and Wenk *et al.* (2020). The total strain tensor (ε_{ij}) is a sum of the dilatational strain tensor (Δ_{ij}), which describes a change in volume of the unit cell, and the deviatoric strain tensor (ε_{ij}'), which describes a change in shape [Fig. 4(*a*)]: $\varepsilon_{ij} = \Delta_{ij} + \varepsilon_{ij}'$, where

$$\Delta_{ij} = \begin{bmatrix} \delta & 0 & 0 \\ 0 & \delta & 0 \\ 0 & 0 & \delta \end{bmatrix}$$

and

$$\varepsilon_{ij}' = \begin{bmatrix} \varepsilon_{11}' & \varepsilon_{12} & \varepsilon_{13} \\ \varepsilon_{12} & \varepsilon_{22}' & \varepsilon_{23} \\ \varepsilon_{13} & \varepsilon_{23} & \varepsilon_{33}' \end{bmatrix}.$$

In our analysis, the deviatoric strain tensor is first transformed from the coordinate system of the diffraction image, a Cartesian coordinate system attached to the unit cell, to the sample coordinate system (x, y, z) using the orientation matrix M and transformation $\varepsilon_{xyz}' = M\varepsilon_{ij}'M^{\rm T}$, such that

$$\varepsilon_{xyz}' = \begin{bmatrix} \varepsilon_{xx}' & \varepsilon_{xy} & \varepsilon_{xz} \\ \varepsilon_{yx} & \varepsilon_{yy}' & \varepsilon_{yz} \\ \varepsilon_{zx} & \varepsilon_{zy} & \varepsilon_{zz}' \end{bmatrix}.$$

An eigen decomposition of ε_{xyz}' provides the geometry of the deviatoric strain ellipsoid in sample coordinates; the eigenvectors are the axes of the ellipsoid scaled by their associated eigenvalues [Fig. 4(*b*)] (Noyan & Cohen, 1987; Tamura, 2014). Negative values are herein defined as compression, and positive values are defined as extension.

2.3. How deviatoric strain is measured and principal stress calculated

The *XMAS* software (Tamura, 2014) determines the crystal orientation and calculates the deviatoric strain tensor for each diffraction image. In this experiment, 1200 diffraction images were collected for each scan. The experimental geometry was refined using the polysilicon calibrant [Fig. 3(*a*)]. The strain is refined from the lattice parameters of the deformed crystal relative to those of unstrained Ti [Fig. 4(*a*)]. The diffraction images are preprocessed by removing bad pixels and background signal due to air scattering and X-ray fluorescence. Next, the reflection positions are located by finding intensity maxima above a certain threshold value, and peaks are fitted with a 2D Gaussian function. Then, each peak is 'indexed' and assigned a corresponding *hkl* plane by triangulation of three peak positions. The crystal orientation can then be derived from the indexing.

The deviatoric strain is calculated by measuring the difference between the observed position of the measured diffraction peaks and the ideal position of peaks calculated for an unstrained lattice. *XMAS* searches for three unique grain orientations per diffraction image using the 'multigrain' setting. If a diffraction image cannot be indexed by *XMAS*, the grain orientation and strain tensor cannot be calculated and the diffraction image is thus excluded from the analysis. After the indexing parameters of a representative Laue image have been optimized for accurate analysis, the rest of the Laue images are automatically processed using the same parameters on a high-performance computing cluster.

The output from *XMAS*, a sequential list file which contains the crystal orientations and strain tensor for every diffraction image indexed, is then loaded into the MATLAB code *XtalCAMP* (Li *et al.*, 2020). The orientation and magnitude of the principal strain axes are calculated for each diffraction image using an eigen decomposition of the deviatoric strain tensor. Strain maps and other visualizations are also plotted using this software. Stress (σ_{ij}) can be calculated from strain (ε_{kl}) by applying Hooke's law: $\sigma_{ij} = C_{ijkl}\,\varepsilon_{kl}$, where C_{ijkl} is the fourth-rank stiffness tensor. We used the experimental stiffness tensor components of monocrystal hexagonal close-packed Ti determined by Dumontet *et al.* (2019). Prior to plotting the strain maps and calculating the principal strains, all diffraction images with fewer than ten indexed reflections were filtered out to eliminate strain measurements with low confidence. Low indexing is probably due to peak distortion from high strain. After filtering, the deviatoric and principal strains were calculated for each diffraction image and the strain maps of the scan area were generated (Figs. 5 and 6). Normalized frequency distributions of equivalent strain and stress were also plotted for each scan using *XtalCAMP* (Fig. 7).

From *XtalCAMP* the orientations of the crystal and the residual strain ellipsoid for each diffraction image, defined by three Euler angles relative to the sample coordinates, were then exported and used by *BEARTEX* (Wenk *et al.*, 1998) to generate 3D orientation distributions and plot corresponding pole figures (Figs. 8 and 9).

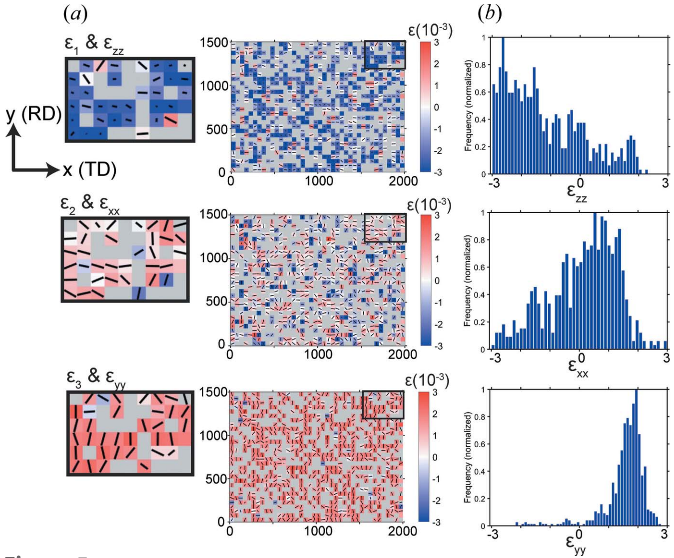

Figure 5
(*a*) Maps showing the magnitude of the ε_{xx}, ε_{yy}, ε_{zz} components of the deviatoric residual strain tensor in sample coordinates (x, y) for Ti_6 scan of dimensions 2000 × 1500 mm with a step size of 50 µm. Projections of principal strain axes ε_1, ε_2 or ε_3 are overlaid onto each pixel as a black line (enlarged inset on left). Each pixel represents one step and shows the data associated with the diffraction image collected at that step. The color of each pixel indicates the deviatoric strain magnitude at that position in millistrains (10^{-3}). Red color (positive values) indicates extension, blue color (negative values) indicates compression. Gray pixels are Laue diffraction images that have fewer than ten indexed reflections and were thus removed from analysis. RD is rolling direction, TD is transverse direction. (*b*) Normalized frequency distributions of residual strain values from plots in (*a*).

3. Results

The µXRD data are most easily understood visually using maps to spatially resolve the data collected from the scanned area. Because the grain size of the sample ranged from 5 to 30 µm in diameter (Fig. 1), and the beam raster step for each scan was 50 µm, grains cannot be resolved in the maps generated (Figs. 5 and 6). Pole figures of strain ellipsoid axes (*i.e.* principal strain axes) are used to compile the data into a 3D representation of residual strain orientation in sample coordinates (Fig. 8).

3.1. Strain

Strain maps for each scan are plotted in Figs. 5 (Ti_6) and 6 (Ti_6_90d). Three maps are displayed for each scan, one for

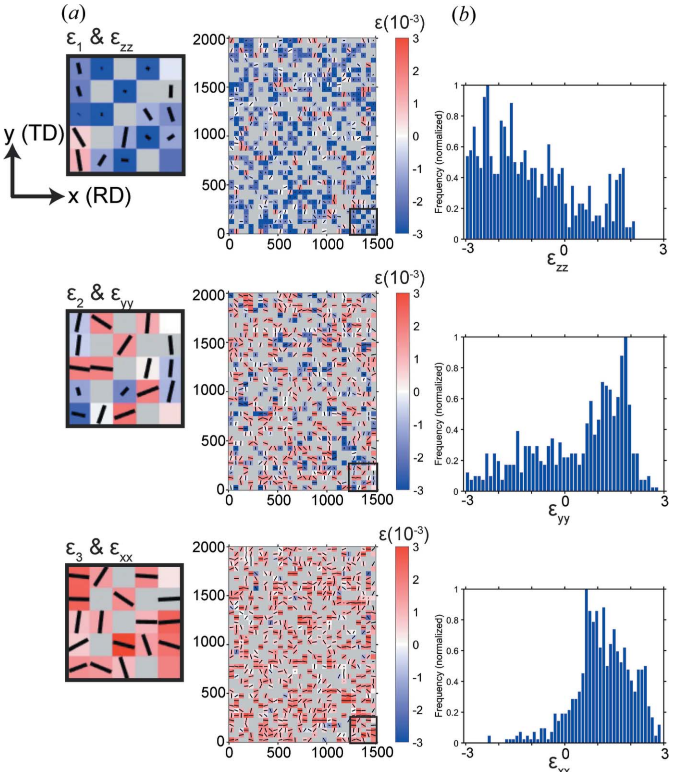

Figure 6
(*a*) Maps showing the magnitude of the ε_{xx}, ε_{yy}, ε_{zz} components of the deviatoric residual strain tensor in sample coordinates (x, y) for Ti_6_90d scan of dimensions 1500 × 2000 mm with a step size of 50 µm. Projections of principal strain axes ε_1, ε_2 or ε_3 are overlaid onto each pixel as a black line (enlarged inset on left). Each pixel represents one step and shows the data associated with the diffraction image collected at that step. The color of each pixel indicates the deviatoric strain magnitude at that position in millistrains (10^{-3}). Red color (positive values) indicates extension, blue color (negative values) indicates compression. Gray pixels are Laue diffraction images that have fewer than ten indexed reflections and were thus removed from analysis. RD is rolling direction, TD is transverse direction. (*b*) Normalized frequency distributions of residual strain values from plots in (*a*).

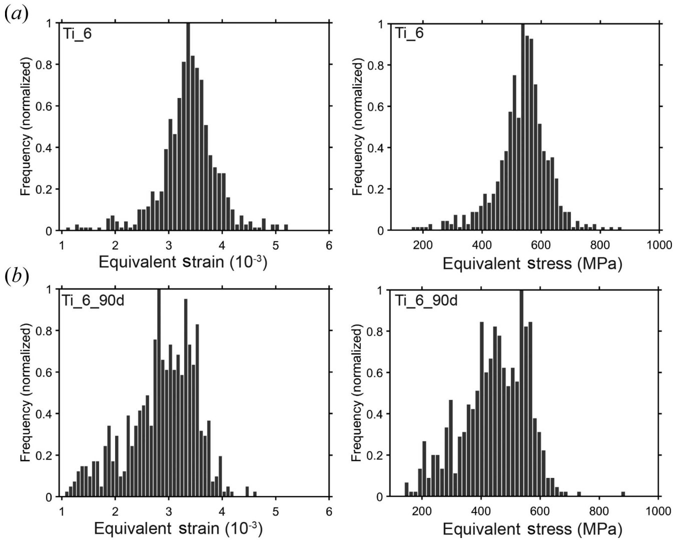

Figure 7
Normalized equivalent strain and stress distributions for Ti_6 (*a*) and Ti_6_90d (*b*).

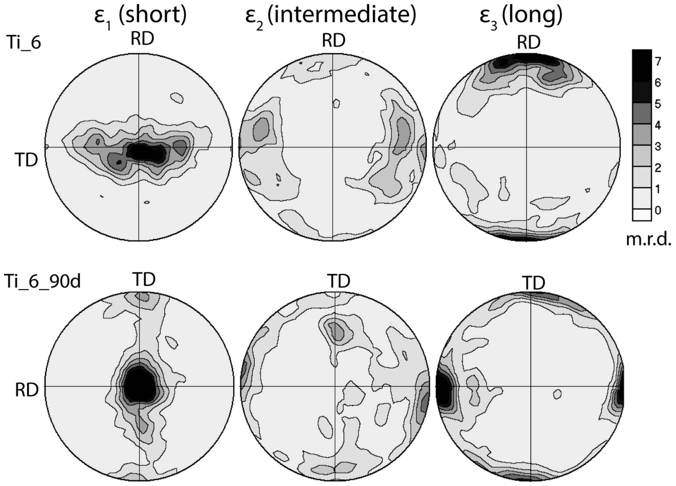

Figure 8
Principal strain axes for Ti_6 (top) and Ti_6_90d (bottom) plotted as pole figures in equal-area projection. Pole figures provide a 3D representation of the principal axes of compression (ε_1), intermediate strain (ε_2) and extension (ε_3) relative to sample coordinates. RD is rolling direction, TD is transverse direction. Contours are in multiples of random distribution (m.r.d.).

each deviatoric strain component (ε_{xx}, ε_{yy} and ε_{zz}) [Figs. 5(*a*) and 6(*a*)]. ε_{xx} is deviatoric strain along the *x* axis, ε_{yy} along the *y* axis and ε_{zz} along the *z* axis. The color of each pixel corresponds to the magnitude of the deviatoric strain component; red indicates positive strain (extension) and blue indicates negative strain (compression). The deviatoric strain values range from −3 to 3 millistrains (10^{-3}). The frequency distributions [Figs. 5(*b*) and 6(*b*)] of the deviatoric strain magnitudes clearly indicate the direction of the most compressive (negative) and most tensile (positive) strain. The strains are most negative in the direction normal to the sample surface (z = ND) for both Ti_6 and Ti_6_90d. The scan for Ti_6 shows the most positive strain in the y = RD direction, while the strain in the x = TD direction spans both positive and negative strain values (Fig. 5). A 90° sample rotation (Ti_6_90d, Fig. 6) results in a 90° strain rotation, with the most positive strain values now in the x = RD direction, and the strain in the y = TD direction spanning positive and negative values.

The projections of the principal strain axes are superposed as black lines onto the color maps. The axis of compression (ε_1) is overlaid onto the map showing the most negative deviatoric strain, and the axis of extension (ε_3) is overlaid onto the map showing the most positive deviatoric strain. Small portions of each scan are enlarged [Figs. 5(*a*) left and 6(*a*) left] to show more clearly the relationship between deviatoric strain magnitude and principal strain axis orientation.

For Ti_6 (Fig. 5), the principal compressive strain (ε_1) shows many axes displayed as dots. This is indicative of a large component in the z direction, as the projection of the normalized principal axis rotates towards the z axis, reducing the visible length of the line to a dot. Other ε_1 axes are oriented horizontally and thus dominated by a component in the x direction. The principal tensile strain (ε_3) axes are mostly vertically oriented and thus parallel with the sample y axis. The intermediate axes (ε_2) are more or less aligned along the x axis as shown by the horizontally oriented lines. For Ti_6_90d (Fig. 6), the principal compressive strain axes also show a larger component in the z direction, displayed by the short, dot-like projections. The principal tensile strain axes are primarily oriented horizontally along the sample x axis, and the intermediate axes are more or less vertically aligned along the sample y axis.

Equivalent strain has been used to estimate the magnitude of the deviatoric strain tensor (Liu, 2005, p. 15, equation 1.29). For both scans, the equivalent strain was calculated to be around 3.25 millistrains (Fig. 7). The 90°-rotated sample has some low equivalent strain values between 1 and 2 millistrains that are absent in the non-rotated sample. The equivalent stress maxima obtained from equivalent strain using Hooke's law for Ti_6 are approximately 575 MPa. The equivalent stress for Ti_6_90d shows a broader distribution with two maxima at approximately 450 and 575 MPa. These fluctuations are probably due to heterogeneous stress distribution and slight variations in scan areas.

The orientations of principal residual strain axes ε_1, ε_2 and ε_3 relative to sample coordinates have been plotted as pole figures using the *BEARTEX* software (Wenk *et al.*, 1998) to provide a 3D visualization of the principal strain axis orientations for each scan (Fig. 8). The pole figures display the 3D distributions of each strain axis in equal-area projection with respect to the sample reference frame. For Ti_6, the principal axes of compression are concentrated parallel to the ND and the principal axes of extension are aligned with the RD. For Ti_6_90d, the principal axes of compression are also oriented parallel to the ND and the principal axes of extension are aligned with the RD, now rotated 90°.

3.2. Deformation texture

The deformation texture measured in the Ti sheet is displayed with (0001) pole figures [Figs. 9(*a*) and 9(*b*)]. The

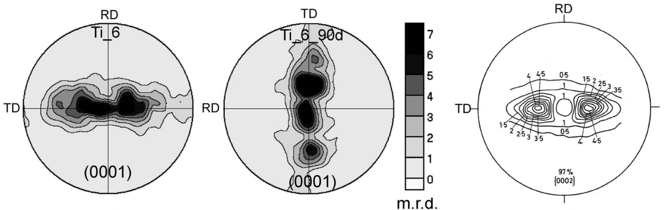

(*a*) (*b*) (*c*)

Figure 9
Deformation textures of crystal (0001) poles plotted as equal-area projection pole figures for Ti_6 (*a*) and Ti_6_90d (*b*). RD is rolling direction, TD is transverse direction. Contours are in multiples of random distribution (m.r.d.). (*c*) Equal-area projection of deformation texture for (0002) poles for rolled Ti reduced to 3% of its original thickness measured with an X-ray pole figure goniometer (Blicharski *et al.*, 1979).

crystal orientation relative to the sample coordinates is determined by *XMAS* for each indexed diffraction image on the basis of the relative peak position. Pole figures are then plotted in equal-area projection using *BEARTEX*. The experimentally determined pole figure for Ti_6 shows a girdle of maxima along the transverse direction with a concentration of (0001) poles aligned close to the ND. The pole figure for Ti_6_90d shows a 90° rotation of the girdle, still located along the transverse direction which is now oriented vertically. The measured deformation textures are consistent with the deformation texture of rolled Ti reduced to 3% of its original thickness [Fig. 9(*c*)] (Blicharski *et al.*, 1979).

4. Discussion

4.1. Stress and strain

Maps and pole figures are used to express the directionality of residual strain measured by μXRD for the rolled Ti sample. The relative magnitude of the deviatoric strain tensor components [Figs. 5(*b*) and 6(*b*)] suggests compression occurred in the direction normal to the sample surface (z), the ND, which agrees with the deformation conditions. The RD is confirmed through observation of a consistent direction of principal extension. In the non-rotated sample, this is the y axis, and in the 90°-rotated sample it becomes the x axis. Similarly, the orientation of the principal strain axes shows that the axis of maximum compression is parallel with the ND, and the axis of maximum extension is parallel with the RD (Fig. 8).

These findings suggest that the residual strain measured by μXRD is consistent with the deformation conditions used to produce rolled Ti. Hooke's law states a direct correlation between the orientation of strain to stress, thus confirming that the directionality of the principal macrostress is coincident with that of the principal strains.

Some diffraction images could not be indexed sufficiently, probably due to high local plastic strain, and thus were not used in the analysis (gray pixels in Figs. 5, 6). Plastic strain distorts the shape of the reflections, and if the reflections are too highly distorted, it is difficult to accurately assign Miller indices. Additionally, recrystallization, another possibility, results in many small grains and thus very small diffracting volumes that produce overlapping low-intensity Laue peaks with many crystallites which are difficult to index. This technique is limited to samples with large enough crystal size and which have also not been severely plastically deformed. To ensure accurate analysis, a minimum number of indexed peaks per diffraction pattern is necessary, and this number is dependent upon the material. Quartz can have upwards of 50 peaks per diffraction pattern from an undeformed sample; other materials like Ti have around 15 peaks per diffraction pattern. Approximately two-thirds of the expected peaks should be indexed for strong confidence in the strain measurement. If indexing is less satisfactory, this is probably due to small crystallite size or high plastic deformation for which alternative techniques would be more successful, such as high-resolution electron backscatter diffraction measurements (Qian *et al.*, 2017). For samples with high amounts of plastic deformation, equations have been developed to estimate the magnitude of strain on the basis of peak shape and size (Ungár *et al.*, 1989; Barabash *et al.*, 2003; Ice *et al.*, 2005*b*).

The variation in stress orientation can be attributed to grain statistics and inhomogeneous stress distribution amongst the grains in the polycrystalline sample; crystal orientation, grain boundary geometries and grain–grain interactions affect how each grain experiences stress (Wilkinson & Dingley, 1992) (Fig. 1). Additionally, only a small portion of the overall sample was measured during this experiment and, due to the large grain size, poor grain statistics could distort the representation of strain in this sample. This is the likely cause of the broadness of strain distributions around their maxima [Figs. 5(*b*), 6(*b*) and 8].

The equivalent stress calculations show a maximum between 400 and 600 MPa (Fig. 7). This is similar in magnitude to residual stress measured in a Ti–Al–V alloy [Fig. 10 of Wang *et al.* (2020)] and low-Fe Ti alloys [Fig. 7.25 of Schajer (2013)]. The broadness of equivalent strain distributions (Fig. 7) and the variation in ε_{zz} distribution [Figs. 5(*b*) and 6(*b*)] could be due to slight variations in the areas scanned as a result of the manual 90° sample rotation and thus different grains being measured. This could be ameliorated with the use of fiducial markers indicating scan start and stop points. A smaller raster step size would also decrease the variability in strain measured because of slight differences in the scanned area between sample rotations. Additionally there will be some variation in the strain measured [Figs. 5(*b*) and 6(*b*)] because the diffraction images and the optimized indexing routine are unique for each scan. Indexing parameters optimized for both scans could be averaged and applied such that the treatment of Laue diffraction images is identical for both scans, which could eliminate any variation in stress due to slight variations in indexing caused by optimization.

4.2. Deformation texture

The (0001) pole figures for both scans are consistent with the deformation texture of rolled Ti (Fig. 9). Compared with the work of Blicharski *et al.* (1979), our images are more irregular, which we attribute to grain statistics with relatively few grains in relation to pole figure goniometry, and representative of a deformation texture reflective of the sample surface rather than the bulk material, as well as inhomogeneous strain distribution in a polycrystalline material (Wilkinson & Dingley, 1992). The deformation textures produced have been attributed to basal and pyramidal slip and twinning (Zaefferer, 2003).

5. Conclusions

Synchrotron X-ray Laue microdiffraction has been used to measure the residual strain for the first time in a sample with known stress history. The directionality of the residual strain agrees with the deformation conditions of the rolled Ti, and the magnitudes of residual strain measured are in agreement with values measured in other studies. This suggests that µXRD and *XtalCAMP* are effective methodologies that could be used to determine the directionality of residual stress reflective of the macroscopic deformation endured by crystalline materials. Our new method of residual strain pole figures provides an approach for a 3D representation of residual strain, analogous to crystallographic pole figures in texture analysis. We also conclude that our predictions of macrostress directionality for quartzite appear to be reliable, thus making quartz a useful ‘paleopiezometer’ to record geological deformation histories. Future work should be done to develop the methodology for materials with different crystal symmetries.

Acknowledgements

This material is based upon work supported by the US Department of Energy, Office of Science Office of Workforce Development for Teachers and Scientists, Office of Science Graduate Student Research (SCGSR) program. The SCGSR program is administered by the Oak Ridge Institute for Science and Education (ORISE) for the DOE. ORISE is managed by ORAU under contract No. DE-SC0014664. All opinions expressed in this paper are the authors’ and do not necessarily reflect the policies and views of DOE, ORAU or ORISE. We thank Kai Chen and Jiawei Kou, both at Xi’an Jiaotong University, and Derek Gobeil from Yokogawa Fluid Imaging Technologies Inc. for their helpful discussions and feedback. We are also appreciative of comments from the editor Professor Dr Jozef Keckes and two anonymous reviewers which helped improve the manuscript. MD acknowledges fellowships from ALS and DOE supporting her research at the Berkeley synchrotron. This research used beamline 12.3.2 which is a resource of the Advanced Light Source, a US DOE Office of Science User Facility under contract No. DE-AC02-05CH11231.

Funding information

The following funding is acknowledged: US Department of Energy, Office of Science (contract No. DE-AC02-05CH1123 to Lawrence Berkeley National Laboratory; award No. DE-SC0014664); National Science Foundation (grant No. EAR2054951; grant No. EAR2154351); US Department of Energy (grant No. DE-FG02-05ER15637).

References

Barabash, R. I., Ice, G. E. & Walker, F. J. (2003). *J. Appl. Phys.* **93**, 1457–1464.

Blicharski, M., Nourbakhsh, S. & Nutting, J. (1979). *Met. Sci.* **13**, 516–522.

Britton, T. B., Dunne, F. P. E. & Wilkinson, A. J. (2015). *Proc. Math. Phys. Eng.* **471**, 20140881.

Cauchois, R., Borbély, A., Gergaud, P., Saadaoui, M. & Inal, K. (2014). *Adv. Mater. Res.* **996**, 930–935.

Chen, K., Kunz, M., Li, Y., Zepeda-Alarcon, E., Sintubin, M. & Wenk, H.-R. (2016). *Geophys. Res. Lett.* **43**, 6178–6185.

Chen, K., Kunz, M., Tamura, N. & Wenk, H.-R. (2011). *Eur. J. Mineral.* **23**, 169–178.

Dumontet, N., Connétable, D., Malard, B. & Viguier, B. (2019). *Scr. Mater.* **167**, 115–119.

Guo, Y., Collins, D. M., Tarleton, E., Hofmann, F., Tischler, J., Liu, W., Xu, R., Wilkinson, A. J. & Britton, T. B. (2015). *Acta Mater.* **96**, 229–236.

Hofmann, F., Song, X., Jun, T.-S., Abbey, B., Peel, M., Daniels, J., Honkimäki, V. & Korsunsky, A. M. (2010). *Mater. Lett.* **64**, 1302–1305.

Hosford, W. F. (2005). *Mechanical Behaviors of Materials*. Cambridge University Press.

Ice, G. E., Larson, B. C., Tischler, J. Z., Liu, W. & Yang, W. (2005*a*). *Mater. Sci. Eng. A*, **399**, 43–48.

Ice, G. E., Larson, B. C., Yang, W., Budai, J. D., Tischler, J. Z., Pang, J. W. L., Barabash, R. I. & Liu, W. (2005*b*). *J. Synchrotron Rad.* **12**, 155–162.

Jiang, T., Wu, C., Tamura, N., Kunz, M., Kim, B. G., Son, H.-Y., Suh, M.-S. & Im, J. (2014). *IEEE Trans. Device Mater. Reliab.* **14**, 698–703.

Krawitz, A. D. & Holden, T. M. (1990). *MRS Bull.* **15**, 57–64.

Kwon, E. P., Sato, S., Fujieda, S., Shinoda, K., Kajiwara, K., Sato, M. & Suzuki, S. (2013). *Mater. Sci. Eng. A*, **570**, 43–50.

Levine, L. E., Larson, B. C., Yang, W., Kassner, M. E., Tischler, J. Z., Delos-Reyes, M. A., Fields, R. J. & Liu, W. (2006). *Nat. Mater.* **5**, 619–622.

Li, Y., Chen, K., Dang, X., Zhang, F., Tamura, N., Ku, C.-S., Kang, H. & Wenk, H.-R. (2020). *J. Appl. Cryst.* **53**, 1392–1403.

Liu, A. (2005). *Mechanics and Mechanism of Fracture: an Introduction*. Materials Park: ASM International.

Lonardelli, I., Gey, N., Wenk, H.-R., Humbert, M., Vogel, S. C. & Lutterotti, L. (2007). *Acta Mater.* **55**, 5718–5727.

Lütjering, G. & Williams, J. C. (2007). *Titanium*, 2nd ed. Heidelberg: Springer.

Ma, Z. S., Zhou, Y. C., Long, S. G. & Lu, C. (2012). *Surf. Coat. Technol.* **207**, 305–309.

Mehta, A., Gong, X.-Y., Imbeni, V., Pelton, A. R. & Ritchie, R. O. (2007). *Adv. Mater.* **19**, 1183–1186.

Morawiec, A. (2018). *J. Appl. Cryst.* **51**, 148–156.

Noyan, I. C., Bunn, J. R., Tippett, M. K., Payzant, E. A., Clausen, B. & Brown, D. W. (2020). *J. Appl. Cryst.* **53**, 494–511.

Noyan, I. C. & Cohen, J. B. (1987). *Residual Stress.* New York: Springer.

Noyan, I. C., Huang, T. C. & York, B. R. (1995). *Crit. Rev. Solid State Mater. Sci.* **20**, 125–177.

Partridge, P. G. (1967). *Int. Mater. Rev.* **12**, 169–194.

Qian, D., Xue, J., Zhang, A., Li, Y., Tamura, N., Song, Z. & Chen, K. (2017). *Sci. Rep.* **7**, 2859.

Renversade, L. & Borbély, A. (2017). *J. Appl. Cryst.* **50**, 1144–1157.

Robinson, J. S., Truman, C. E., Pirling, T. & Panzner, T. (2017). *Mater. Sci. Forum*, **905**, 31–39.

Schajer, G. S. (2013). *Practical Residual Stress Measurement Methods.* Chichester: Wiley.

Shen, H., Chen, K., Kou, J., Jia, Z., Tamura, N., Hua, W., Tang, W., Ehrenberg, H. & Doeff, M. (2022). *Mater. Today*, **57**, 180–191.

Spolenak, R., Brown, W. L., Tamura, N., MacDowell, A. A., Celestre, R. S., Padmore, H. A., Valek, B., Bravman, J. C., Marieb, T., Fujimoto, H., Batterman, B. W. & Patel, J. R. (2003). *Phys. Rev. Lett.* **90**, 096102.

Tamura, N. (2014). *Strain Dislocation Gradients from Diffraction*, edited by G. Ice & B. Barabash, Vol. 4, pp. 125–155. Singapore: World Scientific.

Tamura, N., Celestre, R. S., MacDowell, A. A., Padmore, H. A., Spolenak, R., Valek, B. C., Meier Chang, N., Manceau, A. & Patel, J. R. (2002). *Rev. Sci. Instrum.* **73**, 1369–1372.

Ungár, T. & Borbély, A. (1996). *Appl. Phys. Lett.* **69**, 3173–3175.

Ungár, T., Groma, I. & Wilkens, M. (1989). *J. Appl. Cryst.* **22**, 26–34.

Ungár, T., Gubicza, J., Ribárik, G. & Borbély, A. (2001). *J. Appl. Cryst.* **34**, 298–310.

Van Puymbroeck, E., Nagy, W., Schotte, K., Ul-Abdin, Z. & De Backer, H. (2019). *Appl. Sci.* **9**, 536.

Wang, F., Men, X., Liu, Y. & Fu, X. (2020). *Simul. Model. Pract. Theory*, **104**, 102121.

Wenk, H.-R., Chandler, B. C., Chen, J., Li, Y., Tamura, N. & Yu, R. (2020). *Geophys. J. Int.* **222**, 1363–1378.

Wenk, H.-R., Matthies, S., Donovan, J. & Chateigner, D. (1998). *J. Appl. Cryst.* **31**, 262–269.

Wilkinson, A. J. & Dingley, D. J. (1992). *Acta Metall. Mater.* **40**, 3357–3368.

Wissink, M. L., Chen, Y., Frost, M. J., Curran, S. J., Rios, O., Sims, Z. C., Weiss, D., Stromme, E. T. & An, K. (2020). *Proc. Natl Acad. Sci. USA*, **117**, 33061–33071.

Withers, P. J. (2007). *Rep. Prog. Phys.* **70**, 2211–2264.

Zaefferer, S. (2003). *Mater. Sci. Eng. A*, **344**, 20–30.